Research on synthetic aperture radar imaging technology of one-dimensional layered rough surfaces*

Ji Wei-Jie(姬伟杰)[a)†] and Tong Chuang-Ming(童创明)[a)b)]

[a)] *Missile Institute of Air Force Engineering University, Xi'an* 713800, *China*
[b)] *State Key Laboratory of Millimeter Waves, Nanjing* 210096, *China*

(Received 17 March 2012; revised manuscript received 4 July 2012)

A quick and exact imaging method for one-dimensional layered rough surfaces is proposed in this paper to study the scattering characteristics of a layered medium that exists widely in nature. The boundary integral equations of layered rough surfaces are solved by using the propagation-inside-layer expansion combined with the forward and backward spectral acceleration method (PILE+FB-SA), and the back scattering data are obtained. Then, a conventional synthetic aperture radar (SAR) imaging procedure called back projection method is used to generate a two-dimensional (2D) image of the layered rough surfaces. Combined with the relative dielectric permittivity of realistic soil, the random rough surfaces with Gauss spectrum are used to simulate the layered medium with rough interfaces. Since the back scattering data are computed by using the fast numerical method, this method can be used to study layered rough surfaces with any parameter, which has a great application value in the detection and remote sensing areas.

Keywords: SAR imaging, layered rough surfaces, PILE+FB-SA, back projection method

PACS: 03.50.De, 03.65.Ge **DOI:** 10.1088/1674-1056/22/2/020301

1. Introduction

The research on electromagnetic scattering of ground and sea surfaces, which has important application in detection and remote sensing areas, has attracted extensive attention. Both approximate and rigorous methods have been developed to tackle this problem, but they are mostly focused on the single-interface problem.[1–7] There are many media with layered rough surfaces in nature. For example, the grassplot, the ocean surface coated by oil, the land with snow and foliage can all be viewed as layered rough surfaces. Thus the research on layered medium with rough surfaces is important and useful.

Much attention has been paid to the scattering of layered rough surfaces in recent years. Many approximate methods have been developed based on a small perturbation method[8] and the reduced Rayleigh equations,[9] both of which are limited to small root-mean-square (RMS) derivation of heights of the interfaces, comparatively to the wavelength. Some approximate methods are based on the geometrical optics approximation[10] and thus require quite large RMS heights. Several numerical methods have been devoted to obtaining a rigorous solution. In Ref. [11], a solution to scattering from a cylinder buried in layered rough interfaces based on the extended boundary condition method (EBCM) and generalized scattering matrix technique was presented. In Ref. [12], a fast method of moments called forward–backward method with spectral acceleration (FB-SA) was presented to calculate electromagnetic wave scattering from layered one-dimensional (1D) rough surfaces. The steepest descent fast multi-pole method (SDFMM) and finite element method (FEM) were also investigated.[13,14] Nevertheless, these methods still have some constraints: the EBCM is limited to small RMS heights; in Ref. [13] "the depth of the underground interface should be less than one free space wavelength to satisfy the quasi-planar structure constraint of the SDFMM", and the convergence domain of the FB-SA is still unclear. In Ref. [15], the propagation-inside-layer expansion (PILE) approach was introduced, which is combined with the banded matrix iterative approach/canonical grid (BMIA/CAG) to calculate the bistatic scattering coefficient from a stack of two 1D rough interfaces separating homogeneous media in Ref. [16].

The SAR imaging techniques have been widely used in other electromagnetic areas as a tool for analysis and understanding of scattering and propagation phenomena. For example, in the studies of natural scattering the high-resolution radar images were used to examine small foliage targets in Ref. [17]. Imaging techniques to assist in separating buried targets from surface clutter are also of interest in subsurface target detection problems.[18] The advantage of an imaging technique for improving understanding motivates the use of high-resolution imaging for studying the rough surface scattering phenomena.[19,20]

The goal of this paper is to generate synthetic aperture radar (SAR) raw data and to construct the corresponding SAR image for layered rough surfaces. First, the boundary integral

*Project supported by the State Key Laboratory Fund of Millimeter Waves, Nanjing, China (Grant No. K201201) and the Natural Science Foundation Research Programs of Shannxi Province, China (Grant No. 2011JM8025).

†Corresponding author. E-mail: jiweijie01@163.com

© 2013 Chinese Physical Society and IOP Publishing Ltd

equations are derived, and the forward-backward spectral acceleration method is combined into PILE (PILE+FB-SA) to calculate the matrix equations. Then the 2D SAR imaging processing is introduced, and the proper window function is chosen to reduce the side-lobe level. Finally, the SAR image of a layered rough surface is generated based on the back scattering field data from 3 GHz–7 GHz under tapered wave illumination, which is computed by PILE+FB-SA. The influences of the moisture content in the soil and the thickness of medium on SAR imaging are investigated.

The advancement of this method is that the backscattering data are calculated by PILE+FB-SA which is a fast numerical method, thus the SAR image of layered rough surfaces with any parameter can be obtained quickly and exactly.

2. Theory and formulation

2.1. Boundary integral equations

The geometry of layered medium with rough surfaces is shown in Fig. 1. The rough layer is invariant along the $\hat{\boldsymbol{y}}$ direction and that the incident wave vector lies in the $(\hat{\boldsymbol{x}},\hat{\boldsymbol{z}})$ plane. Consequently, the problem is 2D and the layer is delimited by two 1D surfaces: the upper surface S_1 defined by the surface equation $z_1 = f_1(x)$, and the lower one S_2 defined by $z_2 = f_2(x)$.

The surfaces separate three homogeneous media: the upper one, $\Omega_0 : (\varepsilon_0, \mu_0)$ considered as air, the middle one, $\Omega_1 : (\varepsilon_1, \mu_1 = \mu_0)$ filling the layer, and the lower one $\Omega_2 : (\varepsilon_2, \mu_2 = \mu_0)$. Vectors $\boldsymbol{k}_\mathrm{i}$ and $\boldsymbol{k}_\mathrm{s}$ are the incidence vector and the scatter direction vector. θ_i is the incidence angle, and θ_s is the scattering angle. The thickness of the middle medium is d.

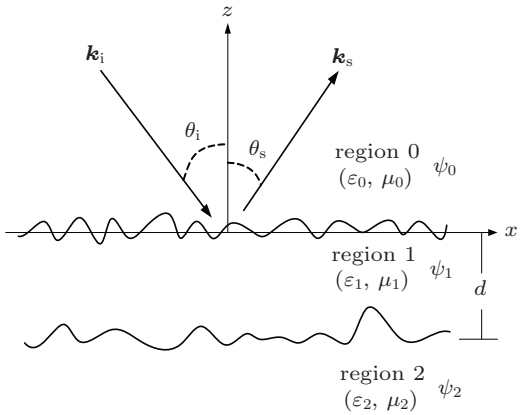


Fig. 1. Geometry of layered rough surfaces.

According to the Huygens surface equivalence principle, we can obtain the following coupled integral equations[12]

$$\frac{\psi_0(\boldsymbol{r})}{2} - \int_{S_1}\left[\psi_0(\boldsymbol{r}')\frac{\partial G_0(\boldsymbol{r},\boldsymbol{r}')}{\partial \boldsymbol{n}'} - G_0(\boldsymbol{r},\boldsymbol{r}')\frac{\partial \psi_0(\boldsymbol{r}')}{\partial \boldsymbol{n}'}\right]\mathrm{d}s' = \psi^{\mathrm{inc}}(\boldsymbol{r}), \quad \boldsymbol{r}\in S_1, \tag{1}$$

$$\frac{\psi_1(\boldsymbol{r}')}{2} - \int_{S_2}\left[\psi_1(\boldsymbol{r}')\frac{\partial G_1(\boldsymbol{r},\boldsymbol{r}')}{\partial \boldsymbol{n}'} - G_1(\boldsymbol{r},\boldsymbol{r}')\frac{\partial \psi_1(\boldsymbol{r}')}{\partial \boldsymbol{n}'}\right]\mathrm{d}s' + \int_{S_1}\left[\psi_1(\boldsymbol{r}')\frac{\partial G_1(\boldsymbol{r},\boldsymbol{r}')}{\partial \boldsymbol{n}'} - G_1(\boldsymbol{r},\boldsymbol{r}')\frac{\partial \psi_1(\boldsymbol{r}')}{\partial \boldsymbol{n}'}\right]\mathrm{d}s' = 0, \quad \boldsymbol{r}\in S_1 \quad \text{or} \quad \boldsymbol{r}\in S_2, \tag{2}$$

$$\frac{\psi_2(\boldsymbol{r})}{2} + \int_{S_2}\psi_2(\boldsymbol{r}')\frac{\partial G_2(\boldsymbol{r},\boldsymbol{r}')}{\partial \boldsymbol{n}'} - G_2(\boldsymbol{r},\boldsymbol{r}')\frac{\partial \psi_2(\boldsymbol{r})}{\partial \boldsymbol{n}'}\mathrm{d}s' = 0, \quad \boldsymbol{r}\in S_2, \tag{3}$$

where ψ^{inc} is the incident field, $G_i(\boldsymbol{r},\boldsymbol{r}')$ are the Green's functions for region i, $G_i(\boldsymbol{r},\boldsymbol{r}') = (\mathrm{i}/4)\mathrm{H}_0^{(1)}(k_0|\boldsymbol{r}-\boldsymbol{r}|)$, $\mathrm{H}_0^{(1)}$ is the zeroth-order Hankel function of the first kind.

The boundary condition on the rough surface is

$$\psi_\mathrm{i}(\boldsymbol{r}) = \psi_{i+1}(\boldsymbol{r}), \quad \frac{\partial \psi_{i+1}(\boldsymbol{r})}{\partial n} = \rho\frac{\partial \psi_\mathrm{i}(\boldsymbol{r})}{\partial n}, \quad (i=0,1), \tag{4}$$

with $\rho = \mu_{i+1}/\mu_i$ for the transverse electric (TE) case and $\rho = \varepsilon_{i+1}/\varepsilon_0$ for the transverse magnetic (TM) case.

To avoid artificial edge diffraction, the tapered plane wave developed by Thorsos[21] is used, which can be expressed as

$$\psi^{\mathrm{inc}}(\boldsymbol{r}) = \exp[\mathrm{i}k(x\sin\theta_\mathrm{i} - z\cos\theta_\mathrm{i}) \times (1+w(x,z))]\exp\left[-\frac{(x+z\tan\theta_\mathrm{i})^2}{g^2}\right], \tag{5}$$

$$w(x,z) = \frac{1}{(kg\cos\theta_\mathrm{i})^2}\left[2\frac{(x_\mathrm{i}+z\tan\theta_\mathrm{i})^2}{g^2} - 1\right], \tag{6}$$

where g is the tapering parameter with the dimension of length and controls the tapering of the incident wave.

2.2. PILE+FB-SA method

The integral equations of layered rough surfaces are discretized by using the method of moment (MoM) with pulse base function. All the surfaces are assumed to be of equal length L, divided into N segments of width $\Delta x = L/N$. We can obtain the following matrix equation

$$\boldsymbol{Z}\boldsymbol{I} = \boldsymbol{V}, \tag{7}$$

where $\boldsymbol{Z}$ is the total impedance matrix of size $4N\times 4N$ $\boldsymbol{I}$, is the unknown vector and equal to

$$\boldsymbol{I}^{\mathrm{T}} = [\boldsymbol{I}_1^{\mathrm{T}} \ \boldsymbol{I}_2^{\mathrm{T}}], \tag{8}$$

with T denoting the transpose operator. $\boldsymbol{I}_1$ and $\boldsymbol{I}_2$ contain the unknown fields $\psi_{1,2}$ and their normal derivatives on the upper and lower surfaces, respectively. The source term $\boldsymbol{V}$ contains information about the incident field

$$\boldsymbol{V}^{\mathrm{T}} = [\boldsymbol{V}_1^{\mathrm{T}} \ \boldsymbol{V}_2^{\mathrm{T}}], \tag{9}$$

with $\boldsymbol{V}_2 = 0$, because the incident field illuminates only the upper surface.

In order to solve the matrix equation efficiently by using the PILE method, the impedance matrix is expressed from sub-matrices as

$$\boldsymbol{Z} = \begin{bmatrix} \boldsymbol{Z}^1 & \boldsymbol{Z}^{2\to 1} \\ \boldsymbol{Z}^{1\to 2} & \boldsymbol{Z}^2 \end{bmatrix}, \tag{10}$$

where $\boldsymbol{Z}^1$ exactly corresponds to the impedance matrix of a single upper interface, $\boldsymbol{Z}^2$ is the impedance matrix of the lower interface, matrixes $\boldsymbol{Z}^{1\to2}$ and $\boldsymbol{Z}^{2\to1}$ can be seen as coupling matrixes between the two interfaces. The complete expression of these matrixes can be found in Ref. [16].

Define the characteristic matrix $\boldsymbol{M}_{\rm c}$ as

$$\boldsymbol{M}_{\rm c} = (\boldsymbol{Z}^1)^{-1} \cdot \boldsymbol{Z}^{2\to1} \cdot (\boldsymbol{Z}^2)^{-1} \cdot \boldsymbol{Z}^{1\to2}. \tag{11}$$

According to the PILE method, the unknown vector of the upper surface can be computed as follows:[15]

$$\boldsymbol{I}_1^{(P_{\rm pile})} = \left[\sum_{p=0}^{P_{\rm pile}} M_{\rm c}^p\right] \cdot (\boldsymbol{Z}^1)^{-1} \cdot \boldsymbol{V}_1 = \sum_{p=0}^{P} \boldsymbol{Y}_1^{(p)}, \tag{12}$$

with

$$\begin{cases} \boldsymbol{Y}_1^{(0)} = (\boldsymbol{Z}^1)^{-1} \cdot \boldsymbol{V}_1, & p = 0, \\ \boldsymbol{Y}_1^{(p)} = \boldsymbol{M}_{\rm c} \cdot \boldsymbol{Y}_1^{(p-1)}, & p > 0. \end{cases} \tag{13}$$

The norm $\|\boldsymbol{M}_{\rm c}\|$ of a complex matrix is defined by its spectral radius, i.e., the modulus of its eigenvalue which has the highest modulus. Expansion (12) is accurate if $\|\boldsymbol{M}_{\rm c}\| < 1$.

On solving Eq. (12), we can obtain field ψ_1 and $\partial\psi_1/\partial n$ on the upper surface. In addition the scattering field in Ω_0 can be calculated as follows:

$$\psi_{\rm s}(\boldsymbol{r}) = \frac{{\rm e}^{{\rm i}k_0 r}}{\sqrt{r}} \psi_{\rm s}^N(\theta_{\rm s}, \theta_{\rm i}), \tag{14}$$

with

$$\begin{aligned} &\psi_{\rm s}^N(\theta_{\rm s}, \theta_{\rm i}) \\ &= \frac{\rm i}{4}\sqrt{\frac{2}{\pi k_0}}\,{\rm e}^{-{\rm i}\pi/4} \\ &\quad \times \int_{S_r} \left[-{\rm i}(\hat{\boldsymbol{n}} \cdot \boldsymbol{k}_{\rm s})\psi_1(x) - \frac{\partial\psi_1(x)}{\partial n}\right] {\rm e}^{-{\rm i}\boldsymbol{k}_{\rm s}\cdot\boldsymbol{r}}\,{\rm d}s, \end{aligned} \tag{15}$$

where $\boldsymbol{k}_{\rm s} = k_0(\sin\theta_{\rm s}\hat{\boldsymbol{x}} + \cos\theta_{\rm s}\hat{\boldsymbol{z}})$ and $\theta_{\rm s}$ is the scattering angle.

The expression for the normalized scattering coefficient with tapered plane wave incidence is given by

$$\gamma(\theta_{\rm s}) = \frac{\left|\psi_{\rm s}^N(\theta_{\rm s}, \theta_{\rm i})\right|^2}{g\sqrt{\pi/2}\cos\theta_{\rm i}\left(1 - \dfrac{1 + 2\tan^2\theta_{\rm i}}{2k_0^2 g^2 \cos^2\theta_{\rm i}}\right)}. \tag{16}$$

The advantage of the PILE method is that the most complex operations, which are $(\boldsymbol{Z}^1)^{-1} \cdot \boldsymbol{u}$ and $(\boldsymbol{Z}^2)^{-1} \cdot \boldsymbol{u}$ ($\boldsymbol{u}$ is a vector), only concern the local interactions on each surface, respectively, upper and lower, and can be calculated by fast numerical methods that already exist for single rough surfaces. Several methods can be used to speed up the matrix–vector product $(\boldsymbol{Z}^{1,2})^{-1} \cdot \boldsymbol{u}$, like, for instance, the BMIA/CAG,[22] the FB-SA method.[23] Considering its good convergence, the FB-SA method is used to speed up the PILE in this paper.

The FB method is used to speed up the calculation of $(\boldsymbol{Z}^{1,2})^{-1} \cdot \boldsymbol{u}$ in order to reduce the complexity to $o(N^2)$ (N in the unknown number) instead of $o(N^3)$ from a direct LU inversion. In the FB approach, the unknown vector $\boldsymbol{x}$ is split into forward and backward contributions. By assuming that the incident wave propagates from left to right, at any given surface point, the forward contribution $\boldsymbol{x}^{\rm f}$ comes from the incident field and also from the radiation of the surface points on the left of the current point. The backward contribution $\boldsymbol{x}^{\rm b}$ comes from the radiation of the surface points on the right of the current point. The equations governing the forward and backward components are then obtained, and an iterative procedure is adopted.

The FB method can be accelerated by a spectral integral. Parameter x_{d0} is defined as the horizontal distance separating the weak interaction from the strong one. And the interactions between surface points are split into strong and weak interactions. In the iterative procedure of the FB method, and for both forward and backward components, the strong interactions are computed exactly, whereas the weak interactions are computed approximately by using a spectral acceleration. The SA is based on a decomposition of the Green's function (the spectral domain representation), for which the contour of integration is deformed into a steepest descent path going through the saddle point. Then, the integral in the spectral domain representation can be approximated by a sum over a limited number of complex angles with an integrand modulus decaying rapidly away from the origin and its phase varying slightly. As a result, the computation is performed only once for each surface point in the iteration since, with the appropriate contour deformation, contributions from a large number of surface points to a single point are evaluated simultaneously. Consequently, the complexity of the FB-SA is $o(N)$. More details about FB-SA can be found in Ref. [23].

2.3. Back Projection algorithm

A 2D SAR image of a deterministic target can be constructed from a set of frequency and angular sweep complex backscatter field data. Let the scattered field data be available over $f_{\rm min}$ to $f_{\rm max}$ frequency band and θ_1 to θ_2 angle band. Then, a radar image of the target is obtained from[19]

$$I(x,z) = \int_{\theta_1}^{\theta_2} \int_{f_{\rm min}}^{f_{\rm max}} G(f,\theta) w(f) w(\theta)\, {\rm e}^{-{\rm i}2\pi f t(\theta)} f\,{\rm d}f\,{\rm d}\theta, \tag{17}$$

where $G(f,\theta)$ is the complex backscatter data in the frequency and angle domains, $w(f)$ and $w(\theta)$ are the weighting functions for frequency and aspect, respectively. The function $t(\theta)$ is given by

$$t(\theta) = \frac{2(x\sin\theta - z\cos\theta)}{c}, \tag{18}$$

where c is the velocity of light. The relationship among x, z, and θ is shown in Fig. 2.

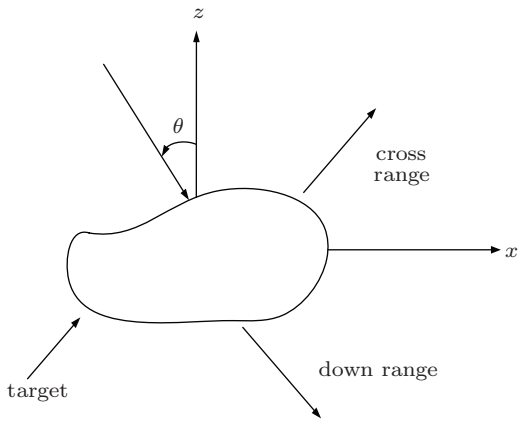


Fig. 2. Imaging geometry for a target.

The weighting function is normalized so that

$$\int f w(f)\,\mathrm{d}f = \int w(\theta)\,\mathrm{d}\theta = 1. \tag{19}$$

By rewriting Eq. (17), we obtain

$$I(x,y) = \int_{\theta_1}^{\theta_2} J(\theta) w(\theta)\,\mathrm{d}\theta, \tag{20}$$

where

$$J(\theta) = \int_{f_{\min}}^{f_{\max}} G'(f,\theta)\,\mathrm{e}^{-\mathrm{i}2\pi f t(\theta)}\,\mathrm{d}f, \tag{21}$$

with

$$G'(f,\theta) = f G(f,\theta) w(f). \tag{22}$$

Equation (21) takes the form of a Fourier transform. Therefore, if the scattered field data are obtained with uniform frequency increments, equation (21) can be evaluated using an inverse Fourier transform (IFFT). Then, $J(\theta)$ is used in Eq. (20) to obtain the complex value of $I(x,z)$.

Considering that the radar data are measured at discrete frequencies and aspect angles, the integrals in Eq. (17) can be rewritten as summations. The radar image is then given by

$$I(x,z) = \sum_{m=1}^{M} \sum_{n=N_1}^{N_2} (n\Delta f) G(n\Delta f, \theta_m) w(n\Delta f) \times w(\theta_m) \exp\left[-\mathrm{i}\frac{4\pi}{c} n\Delta f (x\sin\theta_m - z\cos\theta_m)\right], \tag{23}$$

where Δf is the frequency increment, $N_1 = f_{\min}/\Delta f$ and $N_2 = f_{\max}/\Delta f$. The more aspect angles available to reconstruct the image with a given bandwidth, the better the quality of the resulting image will be.

Down- and cross-range resolutions of the image can be determined by the frequency and angular bandwidth, respectively. The down-range and cross-range resolutions, r_{d} and r_{c} are given by

$$r_{\mathrm{d}} = \frac{c}{2B} \quad \text{and} \quad r_{\mathrm{c}} = \frac{c}{2f_0 \sin\Theta}, \tag{24}$$

where B and Θ represent the frequency bandwidth centred at f_0 and the rotation angle, respectively. To resolve surface variations on the order of a wavelength, backscatter data are typically collected over 4-GHz frequency bandwidth (3 GHz∼7 GHz) and a 40° angular bandwidth corresponding to 3.75 cm down- and 4.67 cm cross-range resolutions in the image domain, respectively.

The unambiguous down- and cross-ranges, D_{d} and D_{c} can be obtained by the following equations

$$D_{\mathrm{d}} = \frac{c}{2\delta_f} \quad \text{and} \quad D_{\mathrm{c}} = \frac{c}{2f_0\delta_\theta}, \tag{25}$$

where δ_{f} and δ_θ denote the steps in frequency and angle, respectively. Step sizes each with 50-MHz ($D_{\mathrm{d}} = 3$ m) frequency and 0.2° ($D_{\mathrm{c}} = 8.6$ m at $f_0 = 5$ GHz) angle are typically used so that image formations with large down-range and cross-range unambiguous regions are possible at normal incidence.

In order to reduce the side-lobe level, an appropriate choice of windows for frequency and angle is necessary. Several well-known window functions are investigated in this paper. For a rectangular window,

$$U(n) = 1 n = 0,1,\ldots,N-1; \tag{26}$$

for a Hamming window,

$$U(n) = 0.54 - 0.46\cos\left(\frac{2\pi n}{N}\right), \quad n = 0,1,\ldots,N-1; \tag{27}$$

for a Blackman window,

$$U(n) = 0.42 - 0.5\cos\left(\frac{2\pi n}{N}\right) + 0.08\cos\left(\frac{4\pi n}{N}\right), \quad n = 0,1,\ldots,N-1. \tag{28}$$

3. Numerical results

3.1. Validation of PILE+FB-SA

Both the upper and lower interfaces are simulated by the random surfaces with Gauss spectrum in this paper. The Gauss spectrum is given by[20]

$$W(k_x) = \frac{\sigma^2 l}{2\sqrt{\pi}}\,\mathrm{e}^{-k_x^2 l^2/4}, \tag{29}$$

where k_x is the spatial spectrum in the x direction, σ is the RMS height, and l is the correlation length.

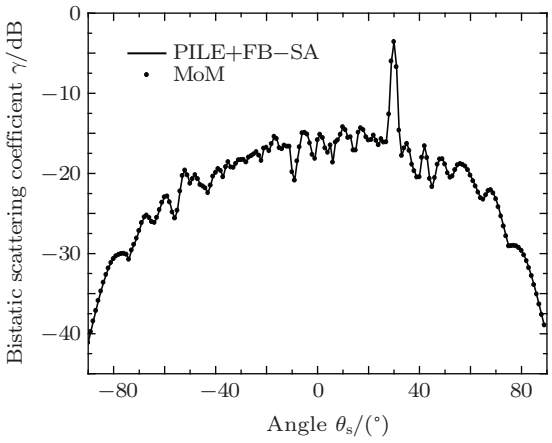


Fig. 3. Bistatic scattering coefficient of layered rough surfaces.

The layered medium is considered to be sand soil. The intermediate and lower soil layer are assumed to have dielectric constants $\varepsilon_1 = 3.73 + 0.15\mathrm{i}$ and $\varepsilon_2 = 4.87 + 0.41\mathrm{i}$ for moisture content values of 5% and 10% at 5 GHz, respectively. The lengths of the two interfaces are both $L = 50\lambda$, and the thickness of the intermediate layer is 2λ. The RMS and correlation length of the upper and lower interfaces are $\sigma_1 = \sigma_2 = 0.1\lambda$, $l_1 = l_2 = 0.5\lambda$. The incident angle is $\theta_i = 30°$, and parameter $g = L/6$.

Figure 3 shows the bistatic scattering coefficient for TM polar incident wave of layered rough surfaces computed by PILE+FB-SA, which is compared with the result of traditional MoM. The result presented in Fig. 3 is the average of 20 Monte Carlo realizations, and each interface is discretized into $N = 1024$ points. The results of PILE+FB-SA are in excellent agreement with those of MoM.

3.2. SAR Image of layered rough surfaces

In this section, we investigate the SAR images of layered rough surfaces. The length of interface is chosen to be $L = 1.98$ m with 1024 unknowns. The RMS and correlation length of the upper and lower interfaces are $\sigma_1 = \sigma_2 = 0.0125$ m, $l_1 = 0.075$ m, and $l_2 = 0.0075$ m, and the thickness of the intermediate layer is 0.1 m. The dielectric constant of each layer soil is the same as that in Subsection 3.1. The frequency band ranges from 3 GHz to 7 GHz centred at 5 GHz with $\delta_f = 100$ MHz. The incidence angle varies from $-20°$ to $20°$ with $\delta_\theta = 0.2°$. A total of 8241 backscattering field data calculations are required.

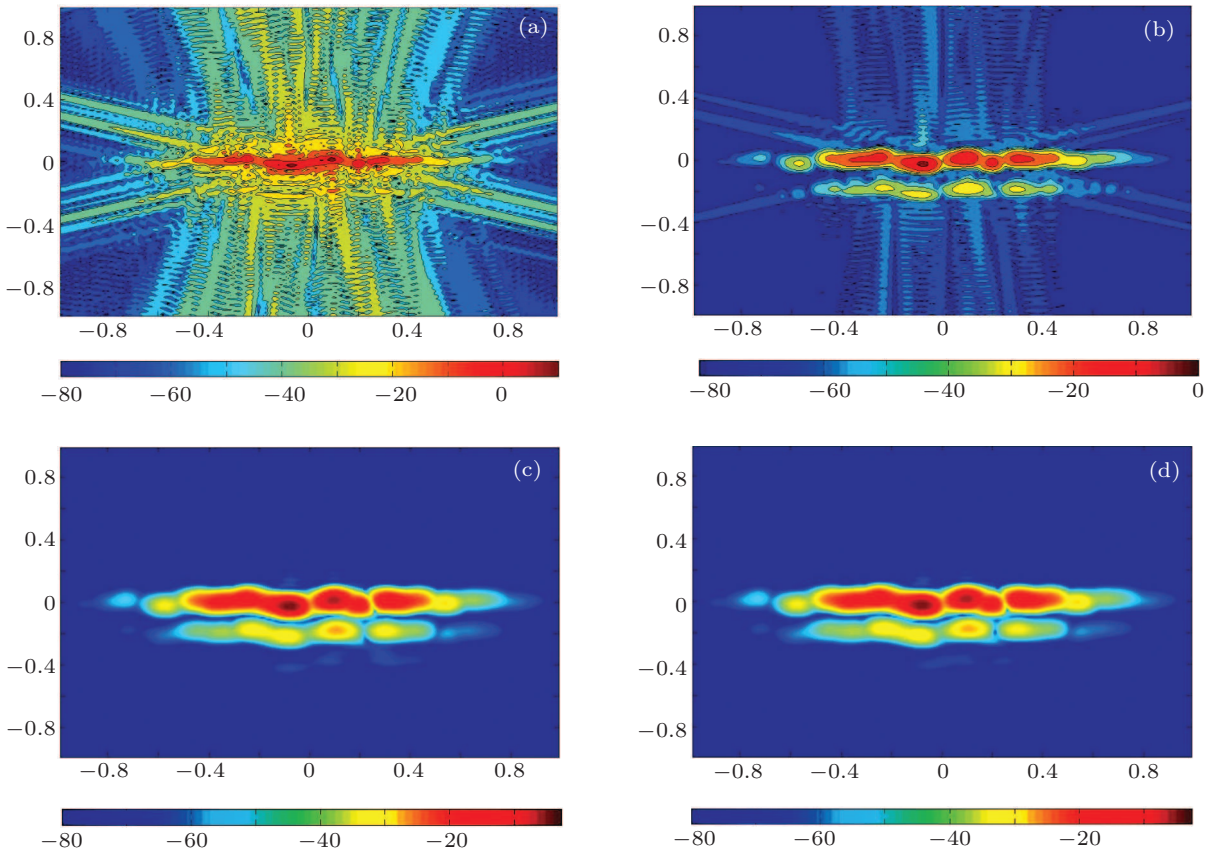


Fig. 4. (color online) The SAR images of layered rough surfaces with different window functions: (a) the VV pol with rectangular window, (b) the VV pol with Hamming window, (c) the VV pol with Blackman window, and (d) the HH pol with Blackman window.

Figures 4(a)–4(c) show the 2D SAR images of layered rough surfaces with different window functions, and the incident wave is of TM polarization (VV pol). Each image is expressed in a dynamic range of 80 dB (−80 dB–0 dB) and composed of 200×200 pixels in 2 m×2 m range so that each pixel size is much smaller than the range resolution. The results show that the image with the rectangular window provides the worst resolution. With the high first side-lobe (−13 dB) and low peak spectrum asymptotic attenuation speed (−6 dB/oct), the rectangular window is not appropriate for discerning multiple scattering effects due to the strong side-lobes. As a result, we nearly cannot find the lower interface from Fig. 4(a). The SAR image with the Hamming window in Fig. 4(b) is better than the result with the rectangular window, but is not enough either. The image with the low first side-lobe (−58 dB) and high peak spectrum asymptotic attenuation speed (−18 dB/oct) Blackman window demonstrates a much improved main-lobe and side-lobe ratio but also reduced resolution. From Fig. 4(c), we can clearly see the images of both the upper and lower rough interfaces, and the mutual effect between them can also be found. Figure 4(d) shows the SAR images of layered rough surfaces with a Blackman window, and the incident wave is of TE polarization (HH pol). The results show that the Blackman window function can give good SAR images of layered rough surfaces for both polarizations.

As shown in the figure, the lower interface image location is different from the actual location. This is because the different dielectric permittivity results in reduced wave velocity and therefore the increased travel time inside the medium. The image location of the sub-layer can be estimated by

$$d' = -\mathrm{Re}(\sqrt{\varepsilon_1})d. \tag{30}$$

The resulting image location of the lower interface is

$$d' \approx -2.1 \times 0.1 = 0.21 \text{ m}.$$

Soil moisture content is a critical factor in determining the scattering level of layered rough surfaces since different moisture content results in different relative dielectric permittivity. Let the moisture content of the intermediate soil layer be 10%, and that of the lower soil layer be 5%. The other parameters are the same as those in Fig. 4. Figure 5 shows the corresponding SAR images of layered rough surfaces. By comparing with Fig. 4, we can see that the SAR image of the lower interface in Fig. 4 is clearer than that in Fig. 5. This is because the relative permittivity of the soil decreases as the moisture content decreases, and higher permittivity results in a higher reflection coefficient.

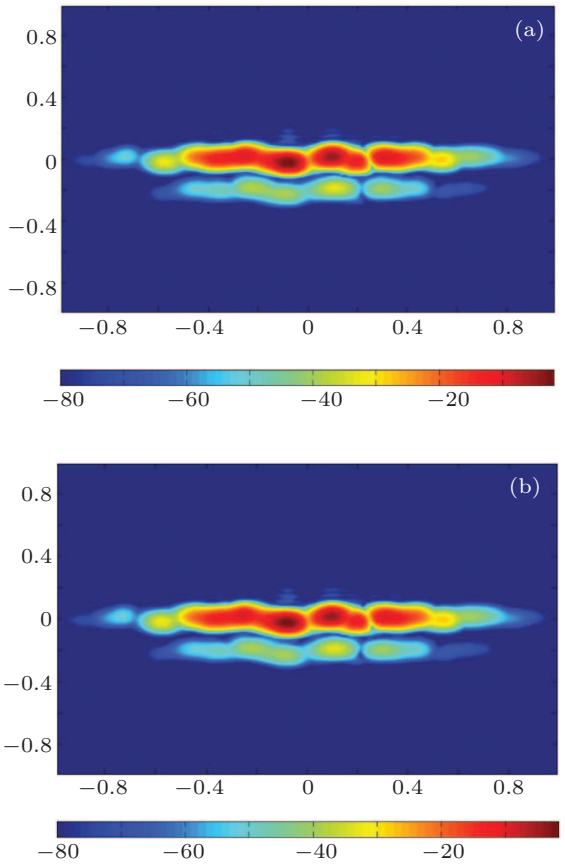


Fig. 5. (color online) The SAR images of layered rough surfaces with different moisture content values. (a) the VV pol and (b) the HH pol.

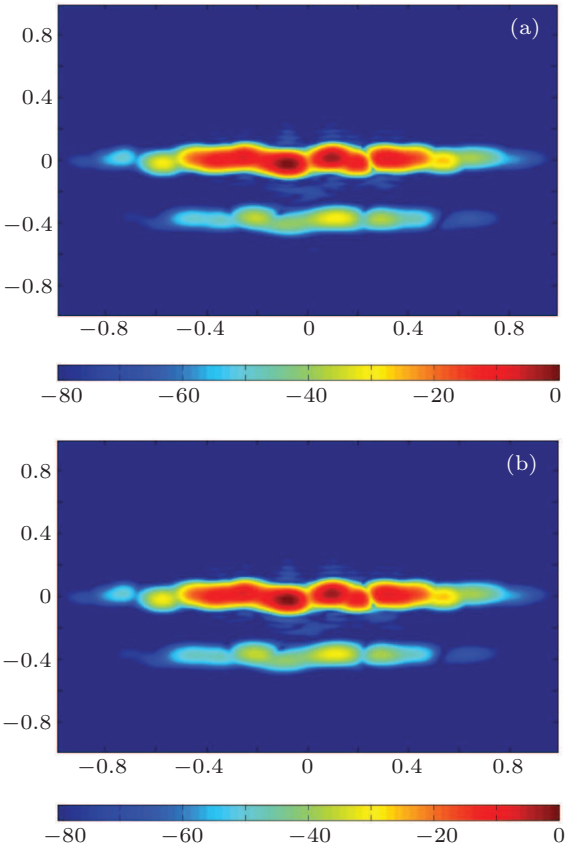


Fig. 6. (color online) The SAR images of layered rough surfaces with $d = 0.2$ m. (a) the VV pol and (b) the HH pol.

Figure 6 shows the SAR images of layered rough surfaces with middle layer medium thickness $d = 0.2$ m for both polarizations. From formula (30), the location of the lower interface is 0.386 m, which is in agreement with that in Fig. 6. From the figure we can know that the brightness of the SAR image of the lower interface is smaller than that in Fig. 4. This is because the attenuation of the electromagnetic wave in medium Ω_1 increases as medium thickness increases.

4. Conclusion

Based on the PILE+FB-SA and the back projection algorithm, a fast SAR imaging method for layered rough surfaces is proposed in this paper. At first, the PILE+FB-SA is used to solve the boundary integral equations of the layered rough surfaces. Then the tomographic processing called back projection algorithm is depicted briefly. Finally, the 2D SAR image of layered soil rough surfaces is obtained by combining the tomographic processing and the back scattering field data calculated by using the PILE+FB-SA. In order to reduce the side-lobe level, the choice of window function is researched. The results show that the Blackman window function can gain good SAR images of layered rough surfaces for both polarizations. The effects of moisture content in the soil and the thickness of the intermediate layer on the SAR image are discussed. The results show that the brightness of the lower interface image decreases as medium thickness increases. This research has an important application value in detection and remote sensing areas.

References

[1] Wang Y Q and Broschat S L 2011 *Waves in Random and Complex Media* **21** 57
[2] Ye H X and Jin Y Q 2006 *IEEE Trans. Geosci. Remote Sens.* **44** 108
[3] Niamsuwan N, Johnson J T and Jezek K C 2011 *Waves in Random and Complex Media* **21** 184
[4] Wang Y H, Zhang Y M, He M X and Guo L X 2008 *Chin. Phys.* B **17** 3696
[5] Toporkov J V and Sletten M A 2007 *IEEE Trans. Geosci. Remote Sens.* **45** 1181
[6] Wang R, Guo L X and Wang A Q 2010 *Acta Phys. Sin.* **59** 3179 (in Chinese)
[7] Zhang Y Q and Ge D B 2009 *Acta Phys. Sin.* **58** 4573 (in Chinese)
[8] Tabatabaeenejad A and Moghaddam M 2006 *IEEE Trans. Geosci. Remote Sens.* **44** 2102
[9] Soubret A G and Bourrely B C 2001 *J. Opt. Soc. Am.* A **18** 2778
[10] Pinel N, Dechamps N, Bourlier C and Saillard J 2007 *Waves in Random Complex Media* **17** 283
[11] Kuo C H and Moghaddam M 2006 *IEEE Tans. Antennas Propag.* **54** 2917
[12] Moss C D, Grzegorczyk T M, Han H C and Kong J A 2006 *IEEE Tans. Antennas Propag.* **54** 1006
[13] El-Shenawee M 2004 *IEEE Trans. Geosci. Remote Sens.* **42** 67
[14] Zhai Y B, Ping X W, Zhou X Y, Zhang J F, Yu W M, Lu W B and Cui T J 2011 *IEEE Trans. Geosci. Remote Sens.* **49** 1431
[15] Dechamps N, Beaucoudrey N D, Bourlier C and Toutain S 2006 *J. Opt. Soc. Am.* A **23** 359
[16] Dechamps N and Bourlier C 2007 *IEEE Trans. Geosci. Remote Sens.* **55** 2790
[17] Fortuny J and Sieber A J 1999 *IEEE Trans. Geosci. Remote Sens.* **37** 1006
[18] Shimada M 2011 *IEEE Trans. Geosci. Remote Sens.* **49** 1712
[19] Kim H and Johnson J T 2002 *IEEE Trans. Antennas Propga.* **50** 94
[20] Alpers W and Huang W G 2011 *IEEE Trans. Geosci. Remote Sens.* **49** 1114
[21] Thorsos A 1988 *J. Opt. Soc. Am.* A **83** 78
[22] Tsang L, Chan C H, Pak K and Sangani H 1995 *IEEE Trans. Antennas Propga.* **43** 851
[23] Chou H T and Johnson J T 2000 *IEEE Trans. Geocis. Remote Sens.* **38** 605